PAPER

Prominence of Cu in a plasmonic Cu–Ag alloy decorated SiO$_2$@S-doped C$_3$N$_4$ core–shell nanostructured photocatalyst towards enhanced visible light activity†

Pradeepta Babu, [a] Soumya Ranjan Dash, [b] Arjun Behera, [a] T. Vijayaraghavan,[c] Anuradha Ashok [c] and Kulamani Parida [*a]

A series of Cu–Ag bimetal alloys decorated on SiO$_2$ and the fabrication of few-layer S-doped graphitic carbon nitride (SC) warped over it to form a core–shell nanostructured morphology have been demonstrated and well characterized through various physiochemical techniques. HRTEM data confirmed the formation of a compact nanojunction between the SiO$_2$ and SC, where Cu–Ag is embedded uniformly with an average particle size of 1.3 nm. The Ag : Cu (1 : 3) between SiO$_2$ and SC produces 1730 μmol h^{-1} g^{-1} of H$_2$ under visible light illumination. Moreover, 6.2-fold current enhancement in the case of Ag : Cu (1 : 3) as compared to the Ag-loaded core–shell nanostructured photocatalyst indicates higher electron–hole-pair separation. The excellent activity was due to the synergistic alloying and plasmonic effect of Ag and Cu. DFT studies reveal that the Cu atom in the Cu–Ag bimetal alloy plays a pivotal role in the generation of H$_2$, and the reaction proceeds *via* a 4-membered transition state. The mechanistic insight proceeds from the generation of hot electrons due to the LSPR effect and their transfer to the SC layer *via* a compact nanojunction.

1. Introduction

Photocatalysis with nanostructured semiconductors[1] has been receiving worldwide attention for environmental remediation and solar energy conversion, akin to photocatalytic H$_2$ generation,[2] which is considered a clean and sustainable process to solve the energy crisis. After the discovery of H$_2$ fuel generation over TiO$_2$ in 1972,[3] this method provided a new direction in the field of clean energy production. However, the UV activity[4] of TiO$_2$, due to its large band gap (3.2 eV) and its high recombination rate of photoinduced electron–hole pairs, severely hinders its practical application. To address the above-described properties of TiO$_2$, a number of semiconductors, such as BiVO$_4$ (ref. 5) and Ag$_3$PO$_4$,[6] have occasionally been demonstrated as visible light-active photocatalysts. In this

context, graphitic carbon nitride[7] (g-C$_3$N$_4$) is gaining enormous attention in the field of visible light H$_2$ generation. Metal-free polymeric catalysts[8] have evoked interest due to their facile fabrication using small organic molecules such as urea or melamine, thermal stability, and solidity in diversified pH media. The suitable conduction band position of the polymer is responsible for the production of H$_2$ upon light irradiation. The simultaneous fabrication of crystalline and N vacancy-rich g-C$_3$N$_4$ showed an increase in photocatalytic H$_2$ generation by the metal free polymeric catalyst.[9] A two-dimensional PCN/2D Ti$_3$C$_2$ MXene interface heterojunction showed an improved hydrogen evolution rate of approximately 2181 μmol^{-1} g^{-1} in comparison to the 3D bulk.[10] The significantly boosted visible-light H$_2$ generation over CN nanosheets has been observed through loading with co-catalysts such as Ni$_3$B/Ni(OH)$_2$, which enhances the charge separation as well as the reduction overpotential.[11] The effort to replace the state-of-the-art cocatalyst, *i.e.* Pt, with cost-effective and abundant transition metal bimetallic alloys such as Pt–M (M = Co, Ni, and Fe) showed enhanced photocatalytic H$_2$ generation by the polymer and by loading a co-catalyst, such as Co$_{1.4}$Ni$_{0.6}$P, an H$_2$ generation value of up to 195 μmol h^{-1} g^{-1} has been achieved.[12] Similarly, a Ni cocatalyst with a shell-layer of 15 nm thickness in a Ni$_3$C@Ni/g-C$_3$N$_4$ photocatalyst produced 16 times higher photocatalytic H$_2$ generation compared to Ni$_3$C/g-C$_3$N$_4$.[13] However, bulk g-C$_3$N$_4$ suffers[14] rapid charge recombination owing to the π–π stacking

[a]Centre for Nanoscience and Nanotechnology (CNSNT), Siksha 'O' Anusandhan, Bhubaneswar 751030, India. E-mail: kulamaniparida@soa.ac.in; paridakulamani@yahoo.com

[b]Physical and Material Chemistry Division, CSIR-NCL Pune, Dr Homi Bhabha Road, Pune 411008, India

[c]Functional Materials Laboratory, PSG Institute of Advanced Studies, Coimbatore, 641004, India

present between the aromatic layers. Again, the stacking of tri-*s*-triazine layers is accountable for the lower specific surface area and consequently for the lower number of active sites for H_2 production. Therefore, some attempts have been made by scientists to fine tune the band gap and enhance the rate of electron–hole pair separation so that the apparent quantum efficiency of the photocatalyst can be enhanced.

Noble metal nanoparticles such as Au and Ag are extensively studied owing to their characteristic localized surface plasmon resonance phenomenon[15] (LSPR). By fine tuning the size and shape of metal nanoparticles,[16] the SPR wavelength can be controlled from the visible to the near infrared region of the solar spectrum. The nanoparticles can competently harvest solar energy and widen the light absorption range so that photoinduced electrons can transfer to the semiconductor through so-called direct energy transfer[17] or resonance energy transfer.[18] The hot electrons[19] generated due to LSPR excitation can be transferred into the neighboring adsorbent or return to the ground state after releasing excess energy to the surroundings. In the case of bimetal[20] plasmonic alloy, an excited hot electron (having an energy of 1–3 eV, which is not in thermal equilibrium with the system) can migrate to the interface depending upon the electronegativity of the metal counterpart. Thus, the bimetal alloy is responsible for the storage of excited electrons, resulting in an increase in electron density that is subsequently useful for enhanced photocatalytic activity. Moreover, synthesis of bimetal alloys can provide a profitable path for the design of cost-effective photocatalysts, where the content of high-cost noble metal nanoparticles can be reduced. Due to the synergistic effect,[21] there is a great improvement in their physical and chemical properties as compared to their monometallic constituents. The formation mechanism[22,23] of alloy nanoparticles is simply the homogeneous mixing of two metals on the atomic scale and is differentiated by their metal to metal bonds. Density functional theory predicts that the synergistic effect[24] of nanoalloys is due to the surface electronic state arising because of the effective atomic coordination number on the surface.[25] Moreover, the construction of the core–shell nanostructure[26] provides a unique platform for the loading of bimetal alloy onto a semiconductor surface.[27] By fine tuning the core size and shell thickness,[28] a number of core–shell nanoparticles can be explored with enhanced photocatalytic activity.[29–33] Core–shell nanostructured photocatalysts are a unique class of nanomaterial possessing a core (inner material) and a shell (outer material) with nanoscale dimensions. The catalytic activity (both photocatalytic and electrocatalytic) depends on the synergistic interaction between the core and shell. Recently, various plasmonic nanoalloys have been demonstrated for photocatalytic processes, such as Au–Ag, Au–Cu, Au–Cu nanostars, and Pt–Au nano alloy. Nalluri *et al.* demonstrated the solvent-free synthesis of an $Fe_2O_3@Au–Ag^{[34]}$ alloy core–shell nanostructured photocatalyst that showed excellent H_2 generation compared to its monometallic Au counterparts. Wang *et al.* synthesized layered double hydroxide supported Au–Cu alloy nanoparticles,[35] which show efficient esterification of benzyl alcohol with methanol. Liu *et al.* fabricated Au–Cu triangular nanostars on CdS[36] by tuning the atomic

ratio of Cu, which showed around threefold H_2 generation compared to CdS. Au–Pt bimetal alloy[37] was decorated on TiO_2 nanorods *via* photo-deposition techniques, and its photocatalytic activity towards benzyl alcohol oxidation was explored. In order to explore the effect of the plasmonic phenomenon on the photocatalytic activity with varying amounts of nickel and silver, Ni and Ag co-modified g-C_3N_4 nanocomposites were fabricated using a photoreduction approach in a mixture of solvent media such as methanol and water, where the 3Ni–1Ag/CN sample produced 2137.5 μmol g^{-1} h^{-1} of H_2.[38] Spinel $ZnFe_2O_4$ microspheres coupled with plasmonic Ag/TiO_2 nanorods were demonstrated to fabricate a Z-scheme heterojunction *via* a facile hydrothermal approach to explore the photocatalytic reduction of CO_2 to CO.[39] Plasmonic Cu-NPs were loaded with a 1D/2D composite of carbon nanotubes modified with protonated carbon nitrides (CNTs/pCN) for photocatalytic conversion of CO_2 to CO.[40] Similarly, plasmonic Au-NPs-embedded Z-scheme WO_3/TiO_2 hetero-junctions were fabricated for photocatalytic H_2 evolution from a glycerol–water mixture, and 0.5% Au-loaded WO_3/TiO_2 produced 4.46-fold higher H_2 evolution compared to WO_3/TiO_2.[41] Further, various photocatalytic systems containing Ag–Cu bimetal alloy as their active plasmonic component are given in Table S1.†

This work demonstrates the fabrication of a series of SiO_2@S-doped graphitic carbon nitride core–shell nanostructured photocatalysts in which Cu–Ag alloy was decorated between the junctions (Scheme 1). The physicochemical properties of the as-synthesized photocatalysts were well characterized using PXRD, HRTEM, FESEM, UVDRS, PL and photocurrent measurements. Further, DFT calculations were performed in order to determine the mechanism behind the water splitting reaction, and the role of Cu in Cu–Ag alloy towards H_2 fuel generation has been explored. The as-synthesized photocatalysts were tested for photocatalytic H_2 fuel generation. The synthesis procedure, characterization, photocatalytic activities and mechanistic insight are discussed in detail.

2. Experimental section

2.1 Reagents

Tetraethyl orthosilicate (TEOS), (3-aminopropyl)triethoxysilane (APTES), sodium borohydride ($NaBH_4$), silver nitrate ($AgNO_3$), copper nitrate hexahydrate ($Cu(NO_3)_2 \cdot 6H_2O$), melamine, thiourea, triethanolamine (TEOA), and sodium sulphate (Na_2SO_4) of analytical grade were obtained from Merck India and used as received. Double distilled water was used throughout the reaction.

2.2 Synthesis of SiO_2 nanoparticle

SiO_2 nanoparticles were prepared using a modified Stober's method described elsewhere.[6] For amine functionalization, 2 g of the as-prepared SiO_2 nanoparticles were dispersed in 100 mL isopropanol, to which 2 mL APTES was added. The resulting solution was refluxed for 2 h, centrifuged and dried at 80 °C overnight.
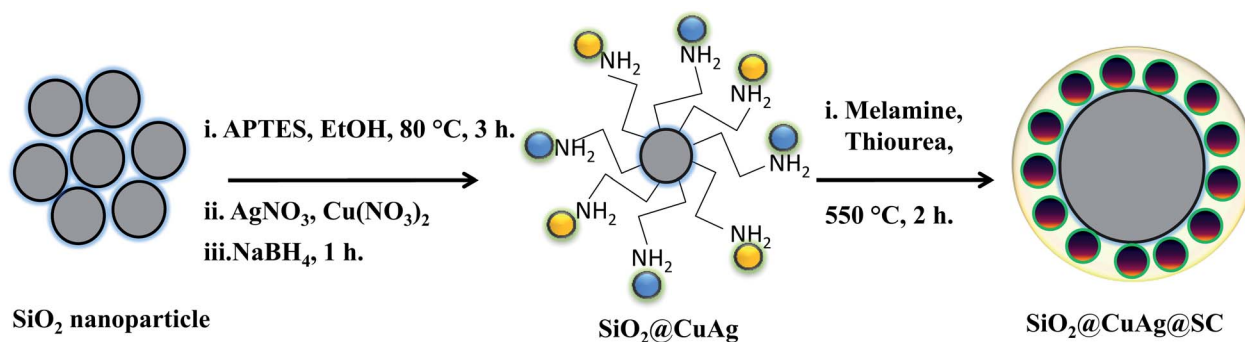
Scheme 1 Synthesis of Ag–Cu bimetal alloy on the SiO_2 surface and fabrication of few-layer SC wrapped over the bimetal alloy.

2.3 Synthesis of SiO_2@AgCu nanoalloy

For the synthesis of SiO_2@AgCu nanoalloy (Ag–Cu-1 : 3), 0.5 g of as-synthesized APTES-functionalized SiO_2 were dispersed in 200 mL water. 20 mg of $AgNO_3$ and 144 mg of $Cu(NO_3)_2$ were added to the above solution, and it was stirred for 15 min to achieve proper dispersion of metal ions. Thereafter, 5 mL of 0.1 M $NaBH_4$ solution was added, which made the colorless solution acquire a light grayish color. The solution was aged for 2 h and then centrifuged to obtain the desired product. The material was dried in an oven overnight. In a similar way, other alloys, such as those with 1 : 1 and 3 : 1 ratios of Ag–Cu, as well as neat Ag and Cu were also loaded on SiO_2.

2.4 Synthesis of SiO_2@AgCu@S-doped C_3N_4

The as-obtained SiO_2@AgCu (100 mg), 300 mg melamine and 300 mg thiourea were ground properly using a mortar and pestle. The as-obtained solid powder was calcined for 2 h at 550 °C in nitrogen atmosphere using a tubular furnace. The as-obtained material was labeled as SCSC-1 : 3. Other alloys containing 1 : 1 and 3 : 1 Ag to Cu ratios were also synthesized by following the same procedure and were labeled as SCSC-1 : 1 and SCSC-3 : 1 for SiO_2@AgCu(1 : 1)@S-doped C_3N_4 and SiO_2@AgCu(3 : 1)@S-doped C_3N_4, respectively. The synthesis protocol is described in Scheme 1. The monometallic counterparts containing only Ag and Cu were synthesized following the same procedure and are labeled SCS and SCC for SiO_2@Ag@S-doped C_3N_4 and SiO_2@Cu@S-doped C_3N_4, respectively. Neat S-doped g-C_3N_4 was fabricated on SiO_2 without loading of the metallic component and was designated as SC.

2.5 Procedure for the photocatalytic reaction

The water splitting reaction was accomplished by dispersing 20 mg of each catalyst in 20 mL water containing 10 vol% triethanolamine (TEOA). The experiment was performed in a homemade quartz batch reactor of 100 mL capacity using a 150 W xenon lamp as the illumination source with a 420 nm cutoff filter. The photoreactor was thoroughly purged with N_2 gas for half an hour prior to irradiation and stirred using a magnetic stirrer for the good dispersion of the catalyst. By adopting the downward displacement of water, the gas evolved from the reactor was collected and analyzed by a gas chromatograph using a thermal conductivity detector. The gas was identified to be H_2.

2.6 Characterization

PXRD of the synthesized materials was performed using a Rigaku MiniFlex diffractometer fitted with Cu Kα radiation (l = 1.45 Å), scanned in the 2θ range from 10 to 80° with a rate of 2° min^{-1}. An HRTEM (JEOL-JEM 2010, Japan) equipped with an energy dispersive X-ray spectrometer was used for the analysis of the morphologies and elemental compositions of the samples. A Krato Axis 165 instrument fitted with a Mg-Kα source was used for the measurement of the XPS spectra of the samples. UVDRS spectra and photoluminescence (PL) spectra were performed on a JASCO UV-Vis spectrophotometer and JASCO-FP-8300 spectrofluorometer in that order. All the electrochemical experiments were performed on an IVIUM-n-STAT instrument, where the electrochemical setup consisted of Pt and Ag/AgCl electrodes as the counter and reference electrode, respectively. For the preparation of the working electrode, the electrophoretic deposition technique was adopted, where 20 mg of every catalyst and iodine were spread in 20 mL acetone and sonicated for 15 min. Fluorine-doped tin oxide (FTO) was dipped in the dispersed medium, and 60 V bias was applied for 6 min for the fabrication of the catalyst on the FTO surface. Prior to conducting the electrochemical experiment, the FTOs were calcined at 200 °C for 2 h in N_2 atmosphere. Linear sweep voltammetry (LSV) was performed by applying potentials from −0.6 to −1.5 V while adapting a scan rate of 25 mV s^{-1}. The photocurrent measurements were performed using a 150 W xenon lamp.

2.7 Computational details

DFT calculations were carried out using the Gaussian 09 program[42] with the B3LYP functional.[43] The 6-31G* basis set[44] was employed for all atoms except silver and copper, for which the effective core potential LanL2DZ basis set[45,46] was used. Harmonic frequency calculations were performed for all stationary points to confirm them as local minima or transition states. Thermal correction and zero point vibration energies were incorporated in the ΔG values. The solvent effect of water

was also taken into consideration by using the polarizable continuum model (PCM) for all the calculations.

3. Results and discussion

3.1 Crystal structure and morphology

Fig. 1(a) shows the typical PXRD pattern of the as-synthesized samples, where SCS shows peaks at 37.8, 43.8, 64.1, and 77.2° that were assigned to the (111), (200), (220), (311) planes of cubic

silver (JCPDS-87-0717), respectively. In the case of SCC, peaks were observed at 43.1, 50.3, and 73.9° and were attributed to the (111), (200), and (220) planes of cubic copper (JCPDS-01-1241), in that order. When Cu–Ag nanoalloy was decorated on the SiO_2 substrate and SC was warped on the alloy, the diffraction peaks shifted more towards the right upon silver incorporation, as found in the case of SCSC-3 : 1, whereas copper incorporation in the alloy shifted the 2θ value slightly towards the right. The peaks were shifted towards the right of the PXRD plot, suggesting the
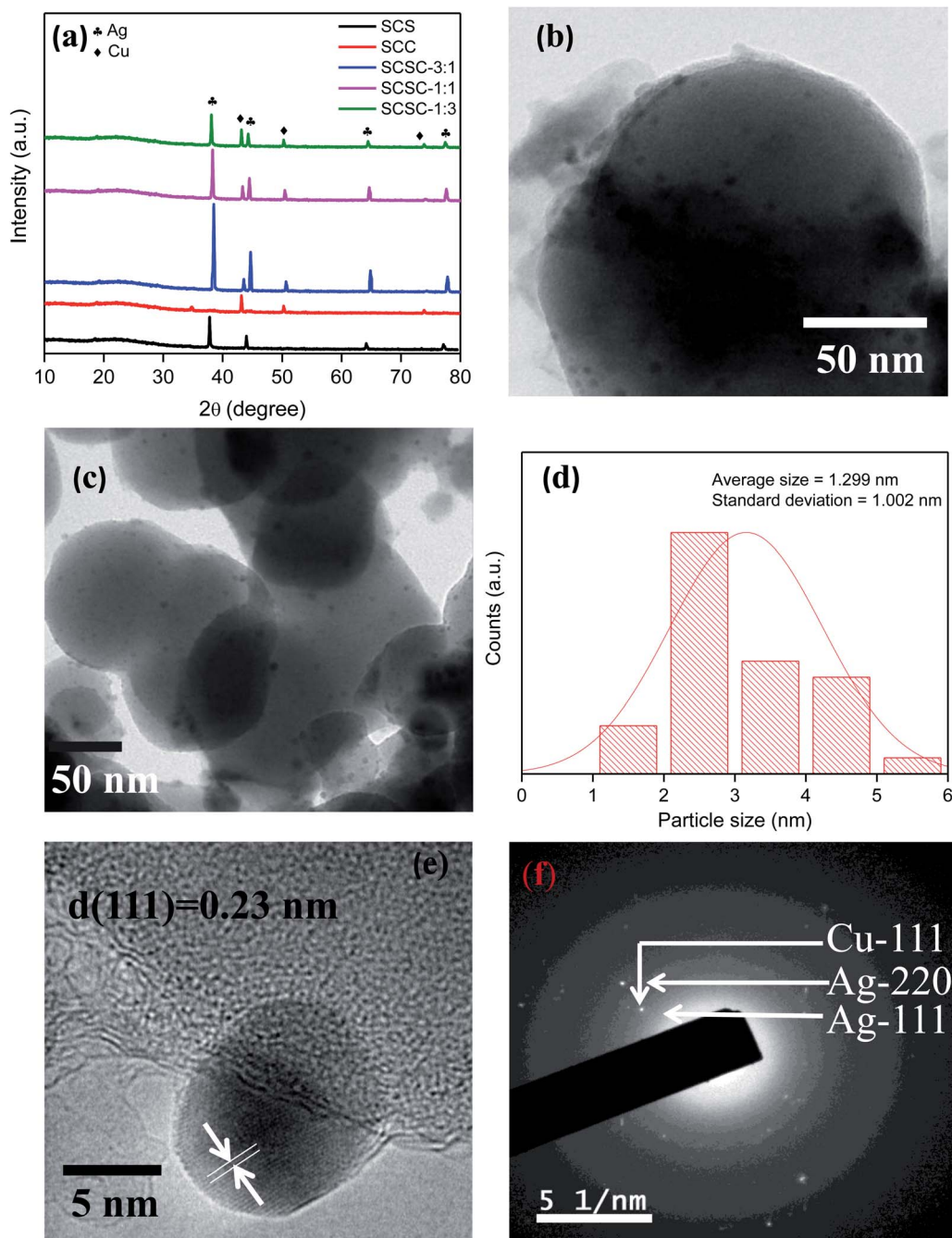
Fig. 1 (a) PXRD of the as-synthesized core−shell nanostructured photocatalyst; (b and c) HRTEM images of SCSC-1 : 3, where SiO_2 as the core and a few layers of SC act as the shell and Cu−Ag bimetal alloy is embedded between the SiO_2 core and SC shell. (d−f) Particle size distribution of Ag−Cu alloy, lattice fringe width of SCSC-1 : 3 matching the d values of the bimetal alloy, and SAED pattern of SCSC-1 : 3.

successful fabrication[47] of Cu–Ag alloy on SiO_2. The Ag (111) and Ag (220) planes were for fcc (Ag) cubic phase, with a lattice parameter $a = 4.076$ Å; moreover, the peak intensity of Ag (111) was found to be strongest, suggesting that the favorable facet for the Cu–Ag nanoalloy is (111). The broad peak at $2\theta = 23.3°$ corresponds to the amorphous structure of SiO_2.[48,49] The crystallite sizes were calculated and found to be 47.7, 38.4, and 32.7 nm in the cases of SCSC-3 : 1, SCSC-1 : 1, and SCSC-1 : 3, respectively. In order to explore the morphology,[50] high resolution transmission electron microscopy (HRTEM) was conducted. From Fig. 1(b), it can be confirmed that SiO_2 nanoparticles around 120 nm in size were successfully synthesized, and few layers of SC with a thickness of around 3–5 nm were warped over it, forming a core–shell nanostructure. Fig. 1(c and d) shows the uniform distribution of the Ag–Cu nanoalloy on the SiO_2 and SC nanojunction, and the particle size of the alloy is 1.3 nm. The homogeneous distribution of Ag–Cu nanoalloy on the SiO_2 surface as well as the close contact between Ag–Cu and SC plays an important role in the enhancement of the photocatalytic activity of SCSC-1 : 3. Fig. 1(e) demonstrates that there was close contact between the SC and nanoalloy, favoring greater exciton separation efficiency. Again, (111) of Ag was the predominant face of the Cu–Ag alloy, and the lattice fringe was 0.23 nm, which is consistent with the PXRD data. The SAED pattern of SCSC-1 : 3 indicates ED spots of the (111) and (220) facets of Ag and (111) of Cu. The SAED data led us to conclude that the alloy particles were not amorphous but polycrystalline in nature (Fig. 1(f)). The weight percent of SCSC-1 : 3 was 2.7 (Ag : Cu-0.5 : 2.2), as depicted in the EDX

spectra (Fig. S1a†). The eutectic temperature[40] of the Ag–Cu alloy was 779.8 °C in N_2 atmosphere, which confirms the thermal stability of the alloy in this work. The XRD and TEM results suggest the successful formation of the core–shell nanostructure, where Ag–Cu alloy was embedded inside the SiO_2 and SC.

3.2 Chemical state analysis

The XPS survey spectrum[51] shows diverse peaks of Si, O, C, N, S, Ag and Cu related to the successful formation of the photocatalyst (Fig. S1b†). The peak at 284.5 eV was considered to be the reference peak for carbon, and peaks were assigned accordingly for the other elements. The XPS peaks of various elements were further deconvoluted using CASA XPS. The core level of C 1s consists of peaks at 284.5 and 287.4 eV, assigned as the adventitious carbon species by the instrument itself and carbon attached to the nitrogen center of carbon nitride, in that order (Fig. 2(a)). Three peaks for N 1s at 397.1, 398.1 and 399.6 eV were attributed to nitride or cyanide, nitrogen attached to the carbon center of carbon nitride, and nitrogen present in the organic matrix, respectively (Fig. S1c†). The core Si 2p has two peaks at 102.3, and 103.2 eV corresponds to the Si–O–Si linkage and Si–O bonding in SiO_2. Similarly, two peaks are present at 531.1 and 532.6 eV for the O 1s core, related to the oxides of Cu and SiO_2, respectively (Fig. 2(b and c)). The S 2p spectrum contains a single peak upon deconvolution at 162.6 eV, which corresponds to the C–S coordination present in the carbon nitride framework (Fig. 2(d)). In the case of the core level of Ag 3d, two peaks were present at 368.1 and 374.1 eV,
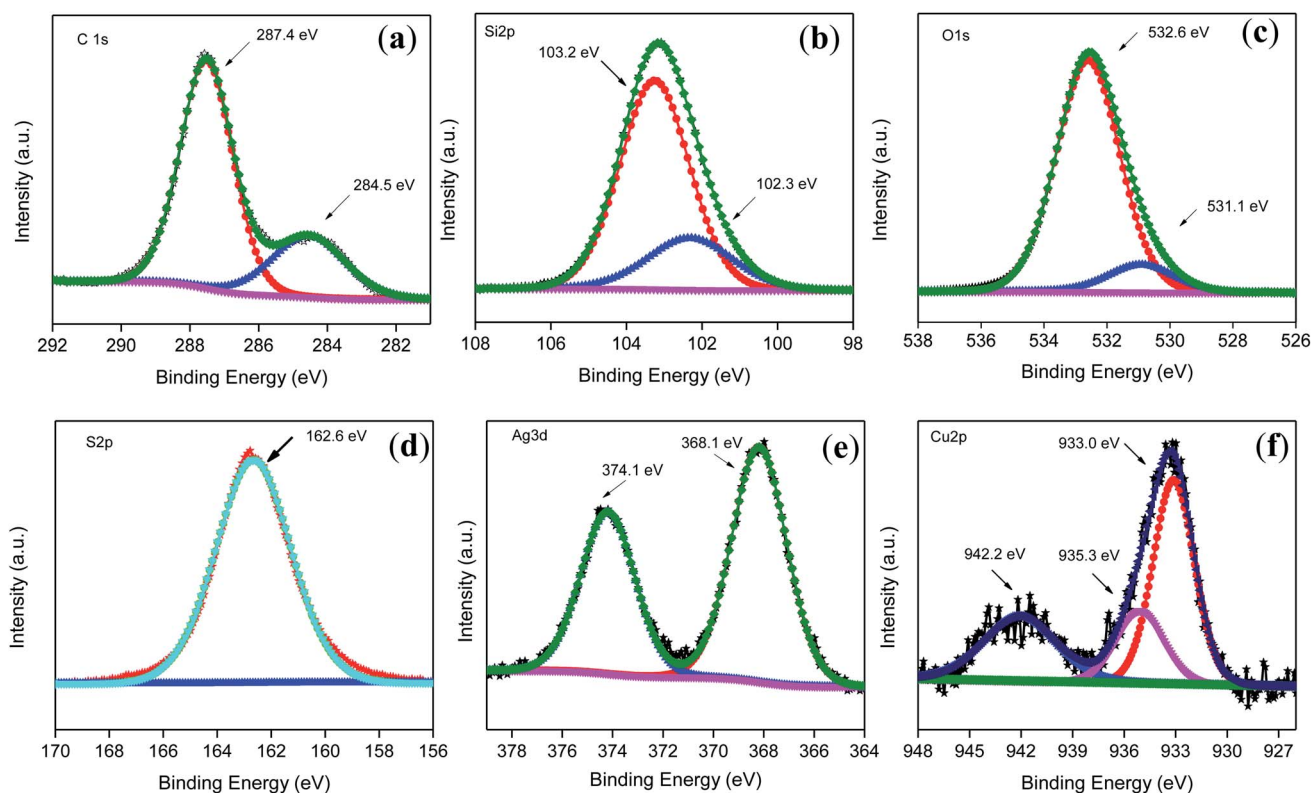

Fig. 2 XPS spectra of SCSC-1 : 3: (a) C 1s, (b) Si 2p, (c) O 1s, (d) S 2p, (e) Ag 3d, (f) Cu 2p.

Paper

related to the $3d_{5/2}$, and $3d_{3/2}$ spin states. The single peak at $3d_{5/2}$ corresponds to the Ag nanoparticles present in the alloy (Fig. 2(e)). Similarly, the XPS core spectrum of Cu 2p shows two peaks at 933.0 and 942.2 eV, which are ascribed to Cu $2p_{3/2}$ and Cu $2p_{1/2}$. The peak present at 942.2 eV is the satellite peak.[52] Cu $2p_{3/2}$ upon deconvolution gives two peaks at 933.0 and 935.3 eV, related to the metallic and +2 oxidation states of Cu, respectively (Fig. 2(f)). The atomic weight percent of Ag–Cu was 1.8% (Ag : Cu-0.45 : 1.03). A greater amount of Cu reduction is possible in the Ag–Cu bimetal alloy compared to the single monometallic Cu nanoparticles due to the alloying effect, as reported in other systems such as ZrO_2.[53]

3.3 Photophysical properties

The optical response of the as-synthesized photocatalysts is portrayed in Fig. 3(a and b). The absorption maxima for SCS and SCC have shifted to the more visible region of the solar spectrum as compared to the bare SC, with a band gap of 2.64 eV. The shifting in the UV-Vis peak is due to the surface plasmon resonance phenomenon (SPR) of Ag and Cu.[54,55] Similarly, in the case of the alloy nanostructures SCSC-3 : 1, SCSC-1 : 1 and SCSC-1 : 3, the absorption peaks were shifted to the more visible region of the solar spectrum, i.e. the absorption band edges for SCS, SCC, SCSC-3 : 1 and SCSC-1 : 1 were 489.0, 567.2, 604.5, and 690.0 nm, respectively, and SCSC-1 : 3 has more visible light absorption, covering the absorption of all the photocatalysts. This represents the full spectrum solar light absorption from UV to Vis to NIR by SCSC-1 : 3, which relates to its excellent catalytic activity. The broad peak in the case of the STSCs is evidence for the formation of a bimetal alloy and not a core–shell structure between Ag and Cu, as the SPR peaks did not appear distinctly for Ag and Cu. The greater photocatalytic activity by the SCSC-1 : 3 catalysts is due to their high visible light absorption, simultaneous alloying effect and surface plasmon resonance phenomenon. Photoluminescence spectroscopy is an important tool[55,56] in order to probe the photo-induced electron–hole-pair generation and separation at the interface of a photocatalyst. Photoluminescence spectroscopy was performed for all photocatalysts at an excitation wavelength

of 330 nm and portrayed in Fig. 3(b). The spectra showed a broad peak at 450 nm in the case of SC, which relates to the band to band transitions. The PL intensity decreased in the order of SC > SCS > SCC > SCSC-3 : 1 > SCSC-1 : 1 > SCSC-1 : 3, as shown in Fig. S1d.† The trends in the PL intensity suggest that the intensity decreases upon an increase in the amount of Cu. The lesser the PL intensity, the greater the electron–hole pair separation and the better the activity of the photocatalyst. The photo-physical properties, including UVDRS and photo-luminescence spectroscopy, suggest that SCSC-1 : 3 is the best photocatalyst among all.

3.4 DFT calculations

To gain further insight into the mechanism towards photo-catalytic H_2 generation, DFT calculations were carried out for the best proposed photocatalyst using Ag_1Cu_3 as a model. A rhombic Ag_1Cu_3 model is predicted, with a ground state spin multiplicity of 1 (Table S2†). All attempts to optimize a tetrahedral ground state of Ag_1Cu_3 failed and converged to a rhombic geometry. As the H_2 evolution catalytic process occurs in water medium, the ability of the Ag_1Cu_3 catalyst to bind with H^+/H as well as water was evaluated alongside natural bond orbital (NBO) analysis (Fig. S2†). From Fig. S2,† it is clear that Cu2 and Cu3 are structurally and electronically similar. Both are potentially the best sites for water and H^+/H binding. However, H^+/H binding is thermodynamically much more favorable compared to water binding, according to the binding energy values. The highest negative charge density on Cu1 atom, as per the NBO analysis, may be the reason for its inability to bind with water and H. Considering that the reaction is occurring in water medium, the possibility of water splitting along with the H_2 evolution mechanism has been investigated. The optimized model of water bound to the Cu3 atom of Ag_1Cu_3 is shown in Fig. 4(a) (left). Here, the water molecule can go on to interact with the neighbor atoms Ag4 as well as Cu1 via a 4-membered transition state. Both of the possible transition states are shown in Fig. 4(a) (right), and it was found that the kinetic barrier for water to interact with the Cu1 atom is 2 kcal mol^{-1} lower than that of Ag4 atom. Hence, the final product of water split into
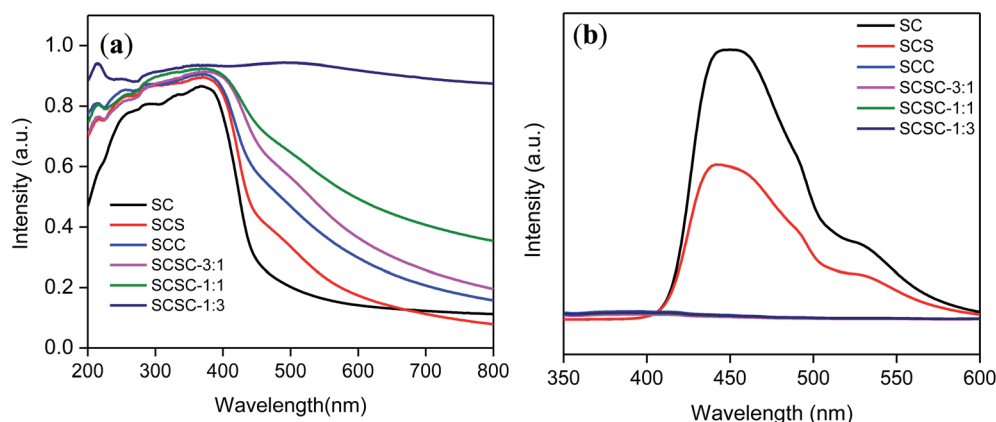

Fig. 3 (a) UV-Vis spectra, (b) photoluminescence spectra of the as-synthesized photocatalysts.
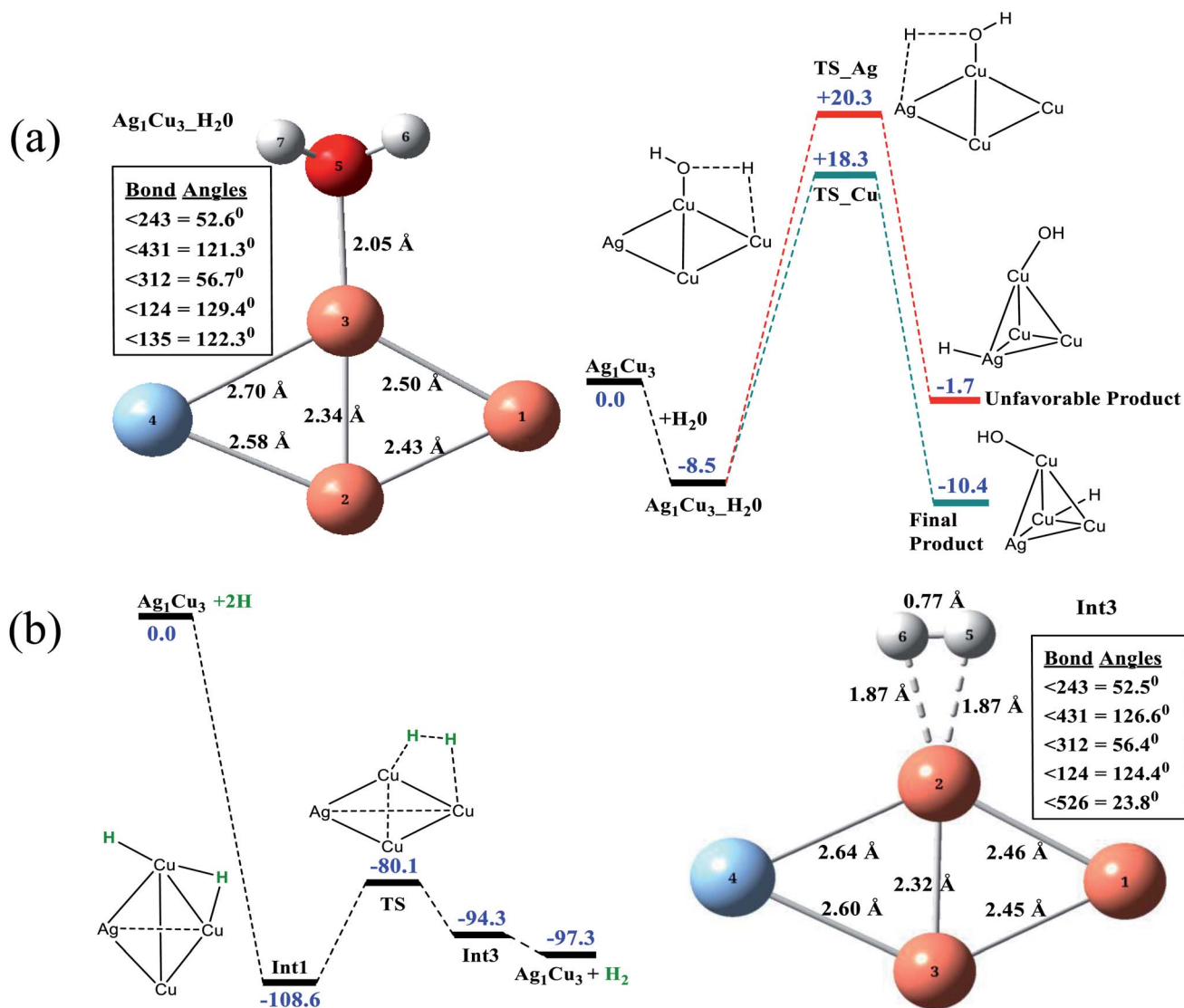
Fig. 4 (a) Left: optimized model of water bound to Cu3 of Ag$_1$Cu$_3$ with the bond parameters. Right: free energy pathway showing water splitting with relative ΔG values (in kcal mol^{-1}). (b) Right: optimized model of Int3 (H$_2$ bound to Cu2 of Ag$_1$Cu$_3$) with the bond parameters, left: free energy pathway showing H$_2$ evolution with relative ΔG values (in kcal mol^{-1}).

OH$^-$ and H$^+$ will proceed through the interaction with Cu1 atom *via* a 4-membered transition state, yielding a tetrahedral geometry where OH$^-$ is bound to Cu3 and H$^+$ is bound to Cu1.

The H$_2$ evolution mechanism for the Pt–Sn system was reported by Chaokong *et al.* We found similar pathways for the Ag$_1$Cu$_3$ system (Fig. 4(b)). Two H$^+$ are adsorbed on the Cu2 atom of Ag$_1$Cu$_3$ and reduced to form Int1 (intermediate-1), which then undergoes a 4-membered transition state with a barrier of 28.5 kcal mol^{-1} to break the interaction between H–Cu1 and result in the formation of Int3 (intermediate-3), as shown in Fig. 4(b) (right). The release of loosely bound H$_2$ from Int3 is found to be thermodynamically favorable by 3 kcal mol^{-1}.

3.5 Photoelectrochemistry

Taking a classical three-electrode system with 0.1 M Na$_2$SO$_4$ solution as the electrolyte, photoelectron chemistry of all the synthesized materials was performed. The linear sweep voltammetry (LSV) plot (Fig. 5(a)) suggests that SCSC-1 : 3 generated 12 mA cm^{-2} current in the cathodic direction. Similarly, other photocatalysts, such as SC, SCS, SCC, SCSC-3 : 1, and SCSC-1 : 1, show 0.04, 1.9, 2.4, 5.7, and 6.3 mA cm^{-2} current in the cathodic direction upon irradiation, respectively. Moreover, the catalyst SCSC-1 : 3 showed current at an onset potential of -1.00 V as compared to the other photocatalysts, which showed current at potentials of -1.45, -1.43, -1.07 and -1.05 for SCS, SCC, SCSC-3 : 1, and SCSC-1 : 1, in that order. The excellent photocurrent generation in the case of SCSC-1 : 3 is attributed to the smaller particle size of bimetal alloy, on the order of 1.3 nm. Gratzel has shown that the particle size is the most important parameter for the photo-electrochemical properties of a semiconductor. A space charge region is not formed when the particle size becomes very small, leading to no exciton
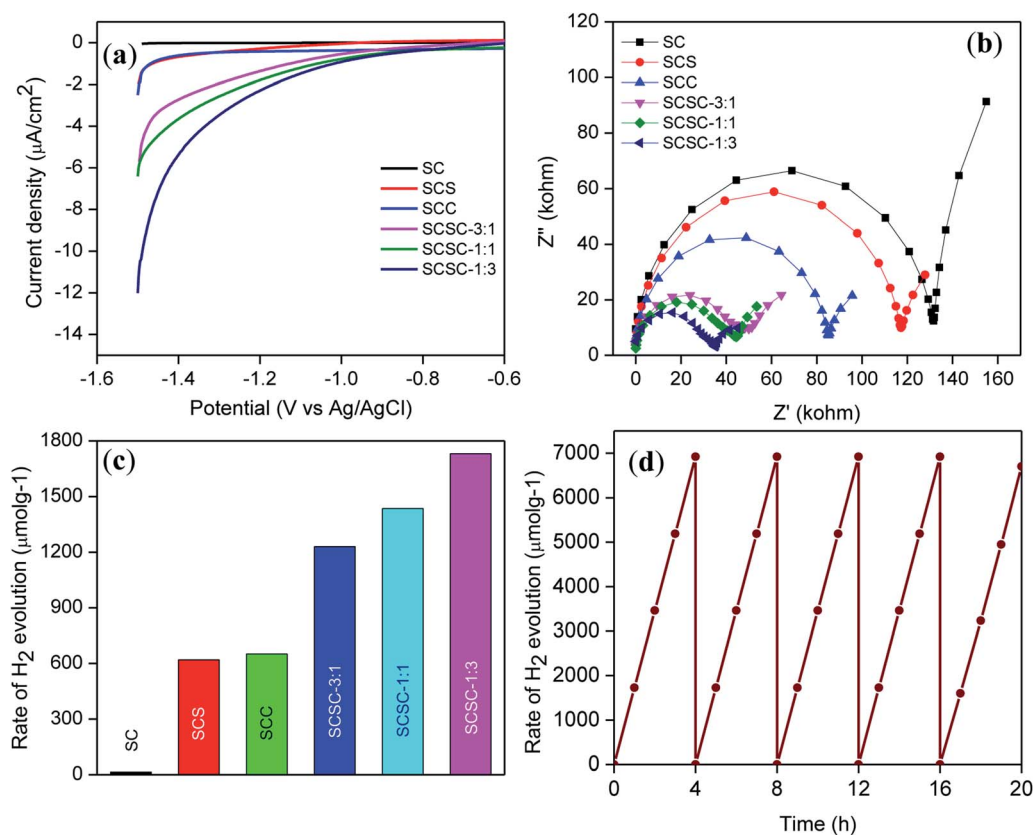
Fig. 5 (a) Linear sweep voltammetry and (b) electrochemical impedance spectra of the as-synthesized photocatalysts. (c) H_2 generation values for all the photocatalysts. (d) Stability test for photocatalytic H_2 evolution.

separation in the semiconductor. In this case, the photocurrent generation is due to the mobility of positive and negative charge carriers. Due to the small size of Ag–Cu, the applied potential was reasonably low for the enhancement in the efficiency of the charge carrier transfer process at the electrode/electrolyte interface. Again, the coating of SC on SiO_2 can act as a channelizer for generation of hot electrons by Ag–Cu and subsequent production of hot holes bellow the Fermi level of Ag–Cu. These hot electrons and holes have sufficient energy to surpass the Schottky barrier, as a result of which Cu–Ag/SC nanojunctions can generate more photocurrent in the cathodic direction. The excellent current generation at lower overpotential by SCSC-1 : 3 relates to its best photocatalytic activity towards H_2 fuel generation.

Electrochemical impedance spectroscopy[57] is a very important tool to explore the charge transfer resistance and ease of electron flow in the semiconductor electrolyte interface as well as the mechanism of the electrochemical reaction. 0.1 M Na_2SO_4 solution was used as an electrolyte and impedance spectroscopy was performed at an applied potential of 0.0 V. The Nyquist plot contains the imaginary part Z' and real part Z'' as the abscissa and ordinate,[5] which relate to the resistance and reactance of the semiconductor,[58] respectively. Fig. 5(b) describes the Nyquist plots of all the photocatalysts, and their values were found to be 131.9, 117.5, 85.0, 47.4, 44.2 and 35.5 Ω for SC, SCS, SCC, SCSC-3 : 1, SCSC-1 : 1 and SCSC-1 : 3, in that

order. The larger arc in the case of SC relates to the high charge transfer resistance, which leads to poor separation of photogenerated electron–hole pairs. The smaller arc in the case of SCSC-1 : 3 relates to the lower charge transfer resistance and higher electrical conductivity. The higher electrical conductivity of the photocatalyst can be corroborated from the LSV data. The decrease in the charge transfer resistance and increase in the electrical conductivity are attributed to the allocation of hot electrons from the Ag–Cu bimetal alloy to SC, thereby inhibiting charge carrier recombination; in all probability, this subsidizes the excellent improvement in the activity. The CB potential of SC[55] has been calculated from the Mott–Schottky plot, and the corresponding VB potential was calculated using the band gap of SC.

3.6 Photocatalytic activity

The catalytic activities of the photocatalysts were explored for the production of H_2 through the water splitting reaction and are depicted in Fig. 5(c). The procedure follows the dispersion of each catalyst in 20 mL of water containing TEOA in a sealed quartz batch reactor. The photocatalysts SC, SCS, SCC, SCSC-3 : 1, SCSC-1 : 1 and SCSC-1 : 3 were able to generate H_2 amounts of 15.2, 620, 652, 1230, 1436, and 1730 μmol h^{-1} g^{-1}, in that order. It can be deduced from the H_2 generation figures that SCSC-1 : 3 can more effectively produce H_2 compared to the other catalysts. Quenching experiments were explored in order

to identify the involvement of active species (Fig. S3†). The experiments were performed in the presence of AgNO$_3$, isopropyl alcohol, TEOA and *p*-benzoquinone as scavengers for electrons, hydroxyl radical, holes and superoxide radical, respectively. The results suggest that electrons are the main active species for the reduction of protons to H$_2$, and the catalyst was also stable up to 4 runs (Fig. 5(d)). The apparent quantum yield was estimated to be 5.2% (band pass filter > 420 nm, 0.3 W irradiatometer). The formula for the apparent quantum yield calculation is

$$AQY(\%) = \frac{2 \times \text{number of H}_2 \text{ molecules}}{\text{number of photons adsorbed}} \times 100$$

The excellent photocatalytic activities of SCSC-1 : 3 were due to the succeeding evidence. From the UV-Vis and PL spectra, it is clear that the photocatalyst can absorb more visible light and exhibit a lower electron–hole recombination rate, respectively. The generation of the high photocurrent value is due to the production of hot electrons through the LSPR process. The interfacial charge transfer process is very high due to the close contact between the Ag–Cu and SC in the case of SCSC-1 : 3, as portrayed from the Nyquist plot. Further, the reusability test of the catalyst towards the water splitting reaction proves the stability of the material, as suggested by PXRD and HRTEM (Fig. S4a–c†).

The size of the plasmonic nanoparticles plays a vital role in the plasmonic performance, and this holds especially true for low band gap semiconductors, where interband excitations occur in wavelength regions which generally overlap with plasmonic resonances. BiVO$_4$ films were decorated with AuNPs of varying size from 10 to 80 nm to study the size dependence of the plasmonic effect.[59] For the excellent visible light photocatalytic activity of Au/TiO$_2$, it was shown that the gold loading and particle size of the gold nanoparticles play important roles in the enhancement of the hydrogen evolution activity with a catalyst containing 0.2 wt% gold with 1.87 nm average particle size.[60] Generally, the plasmonic phenomenon and subsequent ejection of hot electrons occur upon irradiation. In this case, a single semiconductor (S-doped C$_3$N$_4$) is present; therefore, a Schottky junction is established between the alloy and semiconductor. The CB/VB of the semiconductor remains same in the dark as well as upon irradiation. The point is more significant when two different semiconductors (the alloy is not a semiconductor here) are present. Hence, we have shown the pinning of hot electrons upon light irradiation for the nanoalloy as well as silver and copper nanoparticles. We have focused only on the proton reduction reaction, whose reduction potential
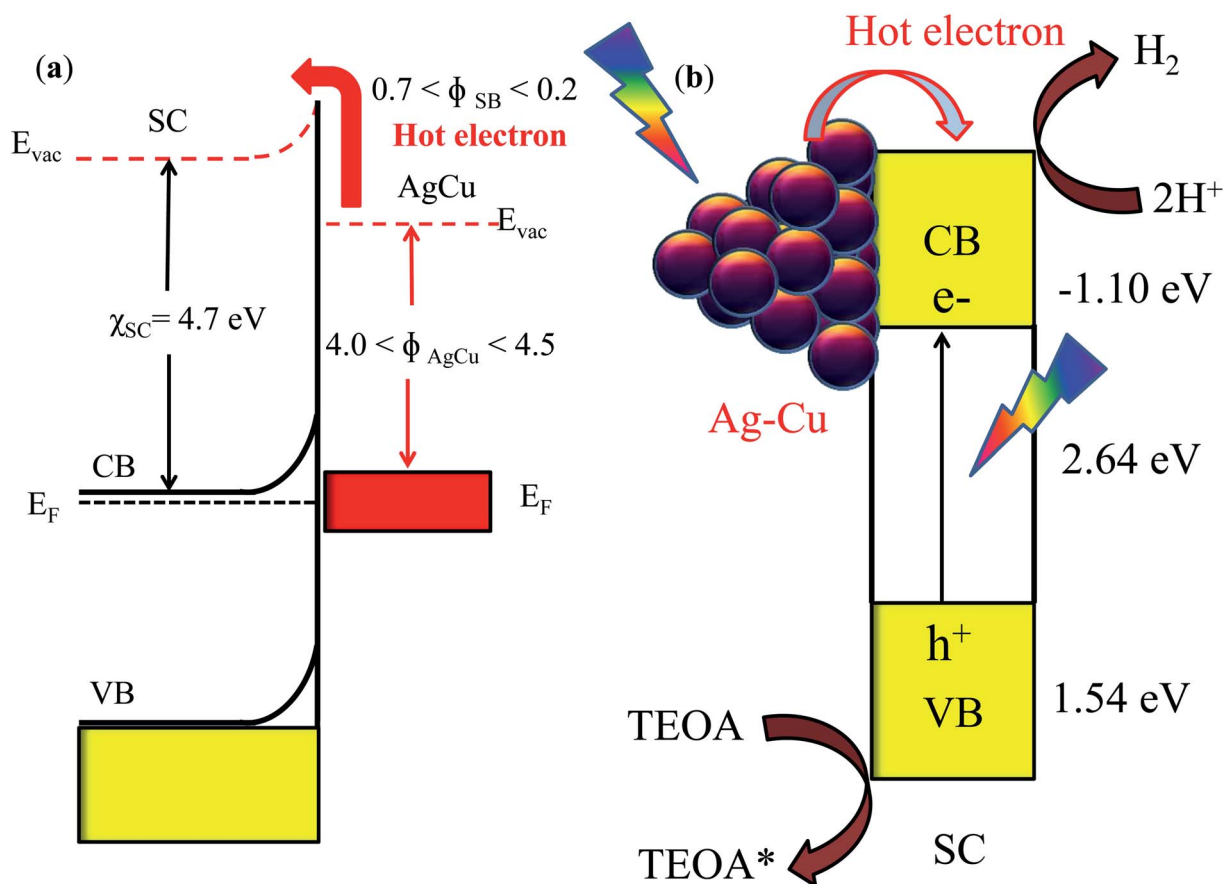
Scheme 2 (a) Energy band diagram of SCSC-1 : 3, where E_F, E_{vac}, χ_{SC}, CB, VB, ϕ_{SB}, and ϕ_{AgCu} represent the Fermi energy level, vacuum energy level, electronegativity of the conduction band of SC, conduction band and valence band of SC, Schottky barrier height, and work function of Ag–Cu nanoalloy, respectively (b) hot electron generation and their participation in proton reduction to produce H$_2$ fuel.

also remains intact before and after irradiation. On the basis of the high photocatalytic activity of the catalyst, a plausible mechanism can be expected and is described in Scheme 2. The mechanism is explained for the individual cases of Ag and Cu and related to the Ag–Cu alloy case. In the SCS system, the Schottky barrier height is estimated to be 0.7 eV, calculated by the difference between the work function of Ag[61] ($\phi = 4.0$ eV) and the electronegativity of the conduction band of SC ($\chi = 4.7$ eV), which is high and subsequently leads to lower photocatalytic activity of SCS (Scheme S1†). In the case of SCC, the Schottky barrier[62] was found to be 0.2 eV (work function of Cu, $\phi = 4.5$ eV), which demonstrates the higher photocatalytic activity of the material by pinning hot electrons *via* LSPR. The excellent photocatalytic activity of SCSC-1 : 3 is explained by the appropriate height of the Schottky barrier[63] (Scheme 2). The work function[64] of the bimetal alloy lies between the work functions of Ag and Cu, which facilitates better electron–hole pair separation by encouraging smooth transfer of hot electrons from the alloy to SC. The VB and CB potentials for SC were calculated according to the equation $E_{VB} = X - E^e + 0.5E_g$, $E_{CB} = E_{VB} - E_g$, where X is the geometric mean of the electronegativity of the constituent atoms, E^e is the energy of a free electron (4.5 eV), and E_g is the band gap energy. The Schottky barrier height was estimated by the difference in the work function of plasmonic metal and the electronegativity of the conduction band of SC, and the mechanism for the photocatalytic activity followed similarly, as described in the literature.[65] Again, the electronegativity of Cu is greater than that of Ag, which leads to charge separation in the alloy; subsequently, electron donation takes place from Ag to Cu. Further, DFT studies revealed the role of Cu in Ag_3Cu_9, which plays an important role in the generation of H_2 fuel from water. The decrease in the photocatalytic activities in the case of SCSC-3 : 1 is due to the presence of a higher amount of Ag. As described in the mechanism, the greater amount of Ag in the bimetal alloy is responsible for the enhancement of the Schottky barrier height and subsequently makes the electron shuttling process difficult. This is due to incomplete mixing of the metal components, which leads to improper band alignment. The photocatalytic activity data suggested that an alloy containing proper amounts of Ag and Cu that are mixed homogeneously can tune the H_2 evolution to a peak as compared to the other synthesized alloys in this work. The molecular mechanism is as follows.

4. Conclusion

In conclusion, a few layers of SC were warped on the surface of SiO_2 to embed Ag–Cu bimetal alloys (with varying Ag to Cu ratios) between them to form a core–shell nanostructure. Out of the various synthesized photocatalysts, SCSC-1 : 3, showed excellent photocatalytic activity towards H_2 fuel (1730 μmol h^{-1} g^{-1}) upon illumination. SCSC-1 : 3 showed excellent visible light absorption due to the synergistic effect of the alloy and plasmonic phenomena. The lowest intensity in the PL spectrum and lowest arc in the Nyquist plot confirmed the better electron–hole pair charge separation and higher electrical conductivity for SCSC-1 : 3, respectively. LSV measurements suggest

that SCSC-1 : 3 can produce 6.2 times more photocurrent in the cathodic direction compared to SCS. Moreover, DFT studies proposed that the Cu atom of Ag_1Cu_3 plays the pivotal role in the generation of H_2, and the reaction proceeds *via* a 4-membered transition state. The excellent activity was accredited to the compact nanojunction between Ag–Cu and SC, where the hot electrons could easily channelize to SC, lowering electron–hole pair recombination. This work provides a suitable demonstration of the design of cost-effective plasmonic bimetallic alloys and their activities towards energy generation.

Author contribution

PB has carried out synthesis, characterization and activity of the photocatalyst and written the manuscript. SRD has performed the DFT calculation. AB has provided assistance during the synthesis. TV and AA have carried out HRTEM analysis. KMP provides overall guidance.

Conflicts of interest

The authors declare no competing financial interest.

Acknowledgements

References

1 M. R. Hoffman, S. T. Martin, W. Choi and D. W. Bahnemann, Photocatalysis over semiconductors, *Chem. Rev.*, 1995, **95**, 69, DOI: 10.1021/cr00033a004.

2 X. Chen, S. Shen, L. Guo and S. S. Mao, Semiconductor-based photocatalytic hydrogen generation, *Chem. Rev.*, 2010, **110**(11), 6503–6570, DOI: 10.1021/cr1001645.

3 B. O'regan and M. Grätzel, A low-cost, high-efficiency solar cell based on dye-sensitized colloidal TiO_2 films, *Nature*, 1991, **353**(6346), 737–740, DOI: 10.1038/353737a0.

4 B. Naik, K. M. Parida and C. S. Gopinath, Facile synthesis of N-and S-incorporated nanocrystalline TiO_2 and direct solar-light-driven photocatalytic activity, *J. Phys. Chem. C*, 2010, **114**(45), 19473–19482, DOI: 10.1021/jp1083345.

5 P. Babu, S. Mohanty, B. Naik and K. Parida, Serendipitous assembly of mixed phase $BiVO_4$ on B-doped g-C_3N_4: an appropriate p–n heterojunction for photocatalytic O_2 evolution and Cr (VI) reduction, *Inorg. Chem.*, 2019, **58**(18), 12480–12491, DOI: 10.1021/acs.inorgchem.9b02309.

6 S. Mohanty, P. Babu, K. Parida and B. Naik, Surface-plasmon-resonance-induced photocatalysis by core–shell $SiO_2@AgNCs@Ag_3PO_4$ toward water-splitting and phenol oxidation reactions, *Inorg. Chem.*, 2019, **58**(15), 9643–9654, DOI: 10.1021/acs.inorgchem.9b00218.

7 X. Wang, K. Maeda, A. Thomas, K. Takanabe, G. Xin, J. M. Carlsson, K. Domen and M. Antonietti, A metal-free

polymeric photocatalyst for hydrogen production from water under visible light, *Nat. Mater.*, 2009, **8**(1), 76–80, DOI: 10.1038/nmat2317.

8 Y. Wang, X. Wang and M. Antonietti, Polymeric graphitic carbon nitride as a heterogeneous organocatalyst: from photochemistry to multipurpose catalysis to sustainable chemistry, *Angew. Chem.*, 2012, **51**(1), 68–89, DOI: 10.1002/anie.201101182.

9 J. Huang, J. Du, H. Du, G. Xu and Y. Yuan, Control of Nitrogen Vacancy in g-C_3N_4 by Heat Treatment in an Ammonia Atmosphere for Enhanced Photocatalytic Hydrogen Generation, *Acta Phys.-Chim. Sin.*, 2020, **36**(7), 1905056.

10 H. Xu, R. Xiao, J. Huang, Y. Jiang, C. Zhao and X. Yang, In situ construction of protonated g-C_3N_4/Ti_3C_2 MXene Schottky heterojunctions for efficient photocatalytic hydrogen production, *Chin. J. Catal.*, 2021, **42**(1), 107–114.

11 L. Xinyong, J. Xie, S. Liu, A. Adamski, X. Chen and X. Li, Low-cost Ni_3B/$Ni(OH)_2$ as an ecofriendly hybrid cocatalyst for remarkably boosting photocatalytic H_2 production over g-C_3N_4 nanosheets, *ACS Sustainable Chem. Eng.*, 2018, **6**(10), 13140–13150.

12 W. Liang, C. Zhu, L. Yin and W. Huang, Construction of Pt-M (M= Co, Ni, Fe)/g-C_3N_4 composites for highly efficient photocatalytic H_2 generation, *Acta Phys.-Chim. Sin.*, 2020, **36**, 1907001, DOI: 10.3866/pku.whxb201907001.

13 S. Rongchen, W. Liu, D. Ren, J. Xie and X. Li, $Co_{1.4}Ni_{0.6}P$ cocatalysts modified metallic carbon black/g-C_3N_4 nanosheet Schottky heterojunctions for active and durable photocatalytic H_2 production, *Appl. Surf. Sci.*, 2019, **466**, 393–400.

14 S. Rongchen, K. He, A. Zhang, N. Li, Y. Hau Ng, P. Zhang, J. Hu and X. Li, In-situ construction of metallic Ni_3C@Ni core–shell cocatalysts over g-C_3N_4 nanosheets for shell-thickness-dependent photocatalytic H_2 production, *Appl. Catal., B*, 2021, **291**, 120104.

15 S. Cao, J. Low, J. Yu and M. Jaroniec, Polymeric photocatalysts based on graphitic carbon nitride, *Adv. Mater.*, 2015, **27**(13), 2150–2176, DOI: 10.1002/adma.201500033.

16 C. Clavero, Plasmon-induced hot-electron generation at nanoparticle/metal-oxide interfaces for photovoltaic and photocatalytic devices, *Nat. Photonics*, 2014, **8**(2), 95–103, DOI: 10.1038/nphoton.2013.238.

17 S. E. Lohse and C. J. Murphy, The quest for shape control: a history of gold nanorod synthesis, *Chem. Mater.*, 2013, **25**(8), 1250–1261.

18 S. K. Cushing, J. Li, F. Meng, T. R. Senty, S. Suri, M. Zhi, M. Li, A. D. Bristow and N. Wu, Photocatalytic activity enhanced by plasmonic resonant energy transfer from metal to semiconductor, *J. Am. Chem. Soc.*, 2012, **134**(36), 15033–15041.

19 J. Li, S. K. Cushing, F. Meng, T. R. Senty, A. D. Bristow and N. Wu, Plasmon-induced resonance energy transfer for solar energy conversion, *Nat. Photonics*, 2015, **9**(9), 601–607.

20 Y. K. Lee, C. H. Jung, J. Park, H. Seo, G. A. Somorjai and J. Y. Park, Surface plasmon-driven hot electron flow probed with metal-semiconductor nanodiodes, *Nano Lett.*, 2011, **11**(10), 4251–4255, DOI: 10.1021/nl2022459.

21 J. Y. Park, Y. Zhang, M. Grass, T. Zhang and G. A. Somorjai, Tuning of catalytic CO oxidation by changing composition of Rh−Pt bimetallic nanoparticles, *Nano Lett.*, 2008, **8**(2), 673–677, DOI: 10.1021/nl073195i.

22 I. Mondal, S. Y. Moon, H. Lee, H. Kim and J. Y. Park, Two-dimensional FeS_2-encapsulated Au: A quasi-epitaxial heterojunction for synergistic catalytic activity under photoelectrocatalytic water reduction, *J. Mater. Chem. A*, 2019, **7**(33), 19258–19268, DOI: 10.1039/C9TA02065A.

23 A. K. Singh and Q. Xu, Synergistic catalysis over bimetallic alloy nanoparticles, *ChemCatChem*, 2013, **5**(3), 652–676, DOI: 10.1002/cctc.201200591.

24 B. Tudu, N. Nalajala, K. Reddy, P. Saikia and C. S. Gopinath, Electronic integration and thin film aspects of Au–Pd/rGO/TiO_2 for improved solar hydrogen generation, *ACS Appl. Mater. Interfaces*, 2019, **11**(36), 32869–32878, DOI: 10.1021/acsami.9b07070.

25 R. Majee, A. Kumar, T. Das, S. Chakraborty and S. Bhattacharyya, Tweaking nickel with minimal silver in a heterogeneous alloy of decahedral geometry to deliver platinum-like hydrogen evolution activity, *Angew. Chem.*, 2019, **59**(7), 2881–2889, DOI: 10.1002/anie.201913704.

26 K. Laasonen, E. Panizon, D. Bochicchio and R. Ferrando, Competition between icosahedral motifs in AgCu, AgNi, and AgCo nanoalloys: a combined atomistic–DFT study, *J. Phys. Chem. C*, 2013, **117**(49), 26405–26413, DOI: 10.1021/jp410379u.

27 S. H. Bae, J. E. Kim, H. Randriamahazaka, S. Y. Moon, J. Y. Park and I. K. Oh, Seamlessly conductive 3D nanoarchitecture of core–shell Ni-Co nanowire network for highly efficient oxygen evolution, *Adv. Energy Mater.*, 2017, **7**(1), 1601492, DOI: 10.1002/aenm.201601492.

28 S. W. Lee, J. W. Hong, H. Lee, D. H. Wi, S. M. Kim, S. W. Han and J. Y. Park, The surface plasmon-induced hot carrier effect on the catalytic activity of CO oxidation on a Cu_2O/hexoctahedral Au inverse catalyst, *Nanoscale*, 2018, **10**(23), 10835–10843, DOI: 10.1039/C8NR00555A.

29 M. B. Gawande, A. Goswami, T. Asefa, H. Guo, A. V. Biradar, D. L. Peng, R. Zboril and R. S. Varma, Core–shell nanoparticles: synthesis and applications in catalysis and electrocatalysis, *Chem. Soc. Rev.*, 2015, **44**(21), 7540–7590, DOI: 10.1039/C5CS00343A.

30 H. Lee, J. Lim, C. Lee, S. Back, K. An, J. W. Shin, R. Ryoo, Y. Jung and J. Y. Park, Boosting hot electron flux and catalytic activity at metal–oxide interfaces of PtCo bimetallic nanoparticles, *Nat. Commun.*, 2018, **9**(1), 1–8, DOI: 10.1038/s41467-018-04713-8.

31 B. Naik, S. M. Kim, C. H. Jung, S. Y. Moon, S. H. Kim and J. Y. Park, Enhanced H_2 generation of Au-loaded, nitrogen-doped TiO_2 hierarchical nanostructures under visible light, *Adv. Mater. Interfaces*, 2014, **1**(1), 1300018, DOI: 10.1002/admi.201300018.

32 M. Kumar, K. Soni, B. Satpati, C. S. Gopinath and S. Deka, Exploration of magnetically separable $Ag@Ag_xNi_y$ core/

graded-alloy-shell nanostructures, *Chem. Commun.*, 2016, **52**(56), 8737–8740, DOI: 10.1039/C6CC04087J.

33 A. B. Vysakh, K. J. Shebin, R. Jain, P. Sumanta, C. S. Gopinath and C. Vinod, Surfactant free synthesis of Au@Ni core-shell nanochains in aqueous medium as efficient transfer hydrogenation catalyst, *Appl. Catal., A*, 2019, **575**, 93–100, DOI: 10.1016/j.apcata.2019.01.017.

34 S. R. Nalluri, R. Nagarjuna, D. Patra, R. Ganesan and G. Balaji, Large scale solid-state synthesis of catalytically active Fe_3O_4@M (M= Au, Ag and Au-Ag alloy) core-shell nanostructures, *Sci. Rep.*, 2019, **9**(1), 1–11, DOI: 10.1038/s41598-019-43116-7.

35 X. Wang, R. Wang, J. Wang, C. Fan and Z. Zheng, The synergistic role of the support surface and Au–Cu alloys in a plasmonic Au–Cu@LDH photocatalyst for the oxidative esterification of benzyl alcohol with methanol, *Phys. Chem. Chem. Phys.*, 2020, **22**(3), 1655–1664, DOI: 10.1039/C9CP05992J.

36 Q. Y. Liu, Y. Zhong, Z. Z. Jiang, K. Chen, S. Ma, F. Wang, W. Wang, L. Zhou and Q. Wang, Controlled growth of triangular AuCu alloy nanostars and high photocatalytic activities of AuCu@CdSheterostars, *J. Mater. Chem. C*, 2020, **8**(14), 4869–4875, DOI: 10.1039/D0TC00098A.

37 X. F. Zhang, Z. Wang, Y. Zhong, J. Qiu, X. Zhang, Y. Gao, X. Gu and J. Yao, TiO_2 nanorods loaded with AuPt alloy nanoparticles for the photocatalytic oxidation of benzyl alcohol, *J. Phys. Chem. Solids*, 2019, **126**, 27–32, DOI: 10.1016/j.jpcs.2018.10.026.

38 S. Fahad, M. Tahir and H. Alias, Synergistic effect of photo-reduced Ni-Ag loaded g-C_3N_4 nanosheets for efficient visible Light Driven photocatalytic hydrogen evolution, *Mater. Sci. Semicond. Process.*, 2022, **137**, 106187.

39 T. Muhammad, Well-designed $ZnFe_2O_4$/Ag/TiO_2 nanorods heterojunction with Ag as electron mediator for photocatalytic CO_2 reduction to fuels under UV/visible light, *J. CO2 Util.*, 2020, **37**, 134–146.

40 T. Muhammad, B. Tahir, M. G. M. Nawawi, M. Hussain and A. Muhammad, Cu-NPs embedded 1D/2DCNTs/pCN heterojunction composite towards enhanced and continuous photocatalytic CO_2 reduction to fuels, *Appl. Surf. Sci.*, 2019, **485**, 450–461.

41 T. Muhammad, M. Siraj, B. Tahir, M. Umer, H. Alias and N. Othman, Au-NPs embedded Z–scheme WO_3/TiO_2 nanocomposite for plasmon-assisted photocatalytic glycerol-water reforming towards enhanced H_2 evolution, *Appl. Surf. Sci.*, 2020, **503**, 144344.

42 M. J. T. Frisch, G. W. Trucks, H. B. Schlegel, G. E. Scuseria, M. A. Robb, J. R. Cheeseman, G. Scalmani, V. Barone, B. Mennucci, G. A. Petersson, H. Nakatsuji, M. Caricato, X. Li, H. P. Hratchian, A. F. Izmaylov, J. Bloino, G. Zheng, J. L. Sonnenberg, M. Hada, M. Ehara, K. Toyota, R. Fukuda, J. Hasegawa, M. Ishida, T. Nakajima, Y. Honda, O. Kitao, H. Nakai, T. Vreven, J. A. Montgomery Jr, J. E. Peralta, F. Ogliaro, M. Bearpark, J. J. Heyd, E. Brothers, K. N. Kudin, V. N. Staroverov, R. Kobayashi, J. Normand, K. Raghavachari, A. Rendell, J. C. Burant, S. S. Iyengar, J. Tomasi, M. Cossi, N. Rega, J. M. Millam,

M. Klene, J. E. Knox, J. B. Cross, V. Bakken, C. Adamo, J. Jaramillo, R. Gomperts, R. E. Stratmann, O. Yazyev, A. J. Austin, R. Cammi, C. Pomelli, J. W. Ochterski, R. L. Martin, K. Morokuma, V. G. Zakrzewski, G. A. Voth, P. Salvador, J. J. Dannenberg, S. Dapprich, A. D. Daniels, Ö. Farkas, J. B. Foresman, J. V. Ortiz, J. Cioslowski and D. J. Fox, *Gaussian 09, Revision A.1*, Gaussian, Inc., Wallingford CT, 2009; A. D. Becke, A half-half theory of density functionals, *J. Chem. Phys.*, 1993, **98**, 1372; C. Lee, W. Yang and R. G. Parr, Development of the Colle-Salvetti correlation-energy formula into a functional of the electron density, *Phys. Rev. B: Condens. Matter Mater. Phys.*, 1988, **37**(2), 785.

43 (*a*) P. C. Hariharan and J. A. Pople, The influence of polarization functions on molecular orbital hydrogenation energies, *Theor. Chim. Acta*, 1973, **28**(3), 213–222; (*b*) R. H. W. J. Ditchfield, W. J. Hehre and J. A. Pople, Self-consistent molecular-orbital methods. IX. An extended Gaussian-type basis for molecular-orbital studies of organic molecules, *J. Chem. Phys.*, 1971, **54**(2), 724–728.

44 D. Andrae, U. Haeussermann, M. Dolg, H. Stoll and H. Preuss, Energy-adjusted *ab initio* pseudopotentials for the second and third row transition elements, *Theor. Chim. Acta*, 1990, **77**(2), 123–141.

45 (*a*) P. J. Hay and W. R. Wadt, Ab initio effective core potentials for molecular calculations. Potentials for the transition metal atoms Sc to Hg, *J. Chem. Phys.*, 1985, **82**(1), 270–283; (*b*) W. R. Wadt and P. J. Hay, Ab initio effective core potentials for molecular calculations. Potentials for main group elements Na to Bi, *J. Chem. Phys.*, 1985, **82**(1), 284–298; (*c*) W. R. Wadt and P. J. Hay, *J. Chem. Phys.*, 1985, **82**(1), 284.

46 (*a*) J. Tomasi and M. Persico, Molecular interactions in solution: an overview of methods based on continuous distributions of the solvent, *Chem. Rev.*, 1994, **94**(7), 2027–2094; (*b*) M. Cossi, G. Scalmani, N. Rega and V. Barone, New developments in the polarizable continuum model for quantum mechanical and classical calculations on molecules in solution, *J. Chem. Phys.*, 2002, **117**(1), 43–54; (*c*) J. Tomasi, B. Mennucci and R. Cammi, Quantum mechanical continuum solvation models, *Chem. Rev.*, 2005, **105**(8), 2999–3094.

47 M. K. Singh, P. Manda, A. K. Singh and R. K. Mandal, Localized surface plasmon behavior of Ag-Cu alloy nanoparticles stabilized by rice-starch and gelatin, *AIP Adv.*, 2015, **5**(10), 107108, DOI: 10.1063/1.4933072.

48 Y. Liang, J. Ouyang, H. Wang, W. Wang, P. Chui and K. Sun, Synthesis and characterization of core–shell structured SiO_2@YVO_4: Yb^{3+}, Er^{3+} microspheres, *Appl. Surf. Sci.*, 2012, **258**(8), 3689–3694, DOI: 10.1016/j.apsusc.2011.12.006.

49 B. Lin, C. Xue, X. Yan, G. Yang, G. Yang and B. Yang, Facile fabrication of novel SiO_2/g-C_3N_4 core–shell nanosphere photocatalysts with enhanced visible light activity, *Appl. Surf. Sci.*, 2015, **357**, 346–355, DOI: 10.1016/j.apsusc.2015.09.041.

50 (*a*) T. Vijayaraghavan, M. Bradha, P. Babu, K. M. Parida, G. Ramadoss, S. Vadivel, A. Selvakumar and A. Ashok,

Influence of secondary oxide phases in enhancing the photocatalytic properties of alkaline earth elements doped LaFeO3 nanocomposites, *J. Phys. Chem. Solids*, 2020, **140**, 109377; (*b*) J. Sopousek, O. Zobac, V. Vykoukal, J. Bursik, P. Roupcova, P. Broz, J. Pinkas and J. Vrestal, Temperature Stability of AgCu Nanoparticles, *J. Nanopart. Res.*, 2015, **17**(12), 478–484.

51 P. Babu and B. Naik, Cu–Ag Bimetal Alloy Decorated $SiO_2@TiO_2$ Hybrid Photocatalyst for Enhanced H_2 Evolution and Phenol Oxidation under Visible Light, *Inorg. Chem.*, 2020, **59**(15), 10824–10834.

52 Y. Wu, Y. Lin and J. Xu, Synthesis of Ag–Ho, Ag–Sm, Ag–Zn, Ag–Cu, Ag–Cs, Ag–Zr, Ag–Er, Ag–Y and Ag–Co metal organic nanoparticles for UV-Vis-NIR wide-range bio-tissue imaging, *Photochem. Photobiol. Sci.*, 2019, **18**(5), 1081–1091, DOI: 10.1039/C8PP00493E.

53 Z. Liu, Y. Huang, Q. Xiao and H. Zhu, Selective reduction of nitroaromatics to azoxy compounds on supported Ag–Cu alloy nanoparticles through visible light irradiation, *Green Chem.*, 2016, **18**(3), 817–825, DOI: 10.1039/C5GC01726B.

54 J. Guo, H. Yu, F. Dong, B. Zhu, W. Huang and S. Zhang, High efficiency and stability of Au–Cu/hydroxyapatite catalyst for the oxidation of carbon monoxide, *RSC Adv.*, 2017, **7**(72), 45420–45431, DOI: 10.1039/C7RA08781K.

55 P. Babu, S. Mohanty, B. Naik and K. Parida, Synergistic effects of boron and sulfur Co-doping into graphitic carbon nitride framework for enhanced photocatalytic activity in visible light driven hydrogen generation, *ACS Appl. Energy Mater.*, 2018, **1**(11), 5936–5947.

56 R. Patil, S. Kelkar, R. Naphade and S. Ogale, Low temperature grown $CuBi_2O_4$ with flower morphology and its composite with CuOnanosheets for photoelectrochemical water splitting, *J. Mater. Chem. A*, 2014, **2**(10), 3661–3668, DOI: 10.1039/C3TA14906D.

57 D. Nelli and R. Ferrando, Core–shell *vs.* multi-shell formation in nanoalloy evolution from disordered configurations, *Nanoscale*, 2019, **11**(27), 13040–13050, DOI: 10.1039/C9NR02963J.

58 S. K. Dutta, S. K. Mehetor and N. Pradhan, Metal semiconductor heterostructures for photocatalytic conversion of light energy, *J. Phys. Chem. Lett.*, 2015, **6**(6), 936–944, DOI: 10.1021/acs.jpclett.5b00113.

59 L. Zhang, L. O. Herrmann and J. J. Baumberg, Size dependent plasmonic effect on $BiVO_4$ photoanodes for solar water splitting, *Sci. Rep.*, 2015, **5**(1), 1–12.

60 C. Gomes Silva, R. Juarez, T. Marino, R. Molinari and H. Garcia, Influence of excitation wavelength (UV or visible light) on the photocatalytic activity of titania containing gold nanoparticles for the generation of hydrogen or oxygen from water, *J. Am. Chem. Soc.*, 2011, **133**(3), 595–602.

61 D. E. Eastman, Photoelectric work functions of transition, rare-earth, and noble metals, *Phys. Rev. B: Solid State*, 1970, **2**(1), 1, DOI: 10.1103/PhysRevB.2.1.

62 R. T. Tung, The physics and chemistry of the Schottky barrier height, *Appl. Phys. Rev.*, 2014, **1**(1), 011304, DOI: 10.1063/1.4858400.

63 J. Tersoff, Schottky barrier heights and the continuum of gap states, *Phys. Rev. Lett.*, 1984, **52**(6), 465, DOI: 10.1103/PhysRevLett.52.465.

64 C. S. Gworek, P. Phatak, B. T. Jonker, E. R. Weber and N. Newman, Pressure dependence of Cu, Ag, and Fe/n-GaAs Schottky barrier heights, *Phys. Rev. B: Condens. Matter Mater. Phys.*, 2001, **64**(4), 045322, DOI: 10.1103/PhysRevB.64.045322.

65 D. Tsukamoto, A. Shiro, Y. Shiraishi, Y. Sugano, S. Ichikawa, S. Tanaka and T. Hirai, Photocatalytic H_2O_2 production from ethanol/O_2 system using TiO_2 loaded with Au–Ag bimetallic alloy nanoparticles, *ACS Catal.*, 2012, **2**(4), 599–603.